Published in final edited form as:
Cancer Res. 2008 October 15; 68(20): 8607–8615. doi:10.1158/0008-5472.CAN-08-0749.

Hyperpolarized ^{13}C Lactate, Pyruvate, and Alanine: Noninvasive Biomarkers for Prostate Cancer Detection and Grading

Mark J. Albers[1,2], **Robert Bok**[2], **Albert P. Chen**[2], **Charles H. Cunningham**[3], **Matt L. Zierhut**[1,2], **Vickie Yi Zhang**[2], **Susan J. Kohler**[4], **James Tropp**[5], **Ralph E. Hurd**[5], **Yi-Fen Yen**[5], **Sarah J. Nelson**[1,2], **Daniel B. Vigneron**[1,2], and **John Kurhanewicz**[1,2]

[1] Department of Bioengineering, University of California San Francisco and University of California Berkeley

[2] Department of Radiology and Biomedical Imaging, University of California San Francisco, San Francisco, California

[3] Sunny Brook Health Sciences Centre, Toronto, Ontario, Canada

[4] Union College, Schenectady, New York

[5] GE Healthcare, Menlo Park, California

Abstract

An extraordinary new technique using hyperpolarized ^{13}C-labeled pyruvate and taking advantage of increased glycolysis in cancer has the potential to improve the way magnetic resonance imaging is used for detection and characterization of prostate cancer. The aim of this study was to quantify, for the first time, differences in hyperpolarized [1-^{13}C] pyruvate and its metabolic products between the various histologic grades of prostate cancer using the transgenic adenocarcinoma of mouse prostate (TRAMP) model. Fast spectroscopic imaging techniques were used to image lactate, alanine, and total hyperpolarized carbon (THC = lactate + pyruvate + alanine) from the entire abdomen of normal mice and TRAMP mice with low- and high-grade prostate tumors in 14 s. Within 1 week, the mice were dissected and the tumors were histologically analyzed. Hyperpolarized lactate SNR levels significantly increased ($P < 0.05$) with cancer development and progression (41 ± 11, 74 ± 17, and 154 ± 24 in normal prostates, low-grade primary tumors, and high-grade primary tumors, respectively) and had a correlation coefficient of 0.95 with the histologic grade. In addition, there was minimal overlap in the lactate levels between the three groups with only one of the seven normal prostates overlapping with the low-grade primary tumors. The amount of THC, a possible measure of substrate uptake, and hyperpolarized alanine also increased with tumor grade but showed more overlap between the groups. In summary, elevated hyperpolarized lactate and potentially THC and alanine are noninvasive biomarkers of prostate cancer presence and histologic grade that could be used in future three-dimensional ^{13}C spectroscopic imaging studies of prostate cancer patients.

Requests for reprints: John Kurhanewicz, University of California San Francisco, Byers Hall, Room 203E, 1700 4th Street, San Francisco, CA 94158-2330. Phone: 415-514-9711; Fax: 415-514-4714; John.Kurhanewicz@radiology.ucsf.edu.

Disclosure of Potential Conflicts of Interest

C.H. Cunningham: Ownership interest, GE Healthcare. D.B. Vigneron: Commercial research grant, GE Healthcare. S.J. Nelson: Commercial research grant, GE Healthcare. J. Kurhanewicz: Commercial research grant, GE Healthcare. The other authors disclosed no potential conflicts of interest.

Introduction

Prostate cancer is now the most commonly diagnosed non-cutaneous cancer in men from the Western world where one of six men will develop prostate cancer during their lifetime.[6] More recently, the use of prostate-specific antigen (PSA) screening and transrectal ultrasound (TRUS)-guided biopsies has led to an increase in early detection of prostate cancer (1). However, the biopsy procedure is moderately invasive and its detection capability is limited by the fact that even with multiple cores only a small percentage of the prostate is sampled. Furthermore, the ensuing treatment decisions pose a great dilemma for patients and their physicians because prostate cancers show a tremendous range in biological diversity and risk. Consequently, prostate cancer is treated with a broad spectrum of approaches from ‘‘active surveillance’’ (regular monitoring without intervention) to aggressive surgical, radiation-based, and other focal therapies (2,3). Currently, the risk assessment of individual patients at diagnosis primarily relies on several clinical variables, including serum PSA, clinical stage (determined by means of digital rectal examination and TRUS), and systematic TRUS-guided biopsy results (number and percentage of positive cores and grade of the cores; ref. 1). Unfortunately, these are often inaccurate or inadequate, particularly when used alone, and often rely on an invasive procedure. Therefore, prostate cancer management, more than is the case for many cancers, requires accurate imaging information to select the most appropriate treatment for an individual patient.

During the last decade, a growing amount of published data has shown that the metabolic biomarkers choline, citrate, and polyamines, provided by three-dimensional proton magnetic resonance spectroscopic imaging (^{1}H MRSI) combined with the anatomic information provided by magnetic resonance imaging (MRI; ref. 4), can significantly improve the clinical assessment of cancer location and extent within the prostate (5–10), extracapsular spread (11,12), and cancer aggressiveness (13,14). Although these metabolic markers are helpful, additional biomarkers could increase the sensitivity of cancer detection and improve the staging of the disease in individual patients.

Recent metabolic studies have indicated that lactate and alanine levels are higher in cancer than in normal tissue (15–17), and this has been associated with increased glycolysis and cell membrane biosynthesis (18,19). ^{18}F-2-deoxy-2-fluoro-D-glucose (FdG) positron emission tomography (PET) studies have shown high rates of glucose uptake in several human cancers and that the glucose uptake correlates directly with the aggressiveness of the disease and inversely with the patient’s prognosis (20,21). The high-glucose uptake leads to increased lactate production in most tumors, although some of them have sufficient oxygen, a condition know as the Warburg effect (22,23) or aerobic glycolysis (18). The increased glycolysis provides the parasitic cancer cells with an energy source that is independent of its oxygen supply, a carbon source for the biosynthesis of cell membranes that begins with lipogenesis (19), and an acid source that likely enables the cells to invade neighboring tissue (18,24). In the case of prostate cancer, FdG-PET uptake has been shown to correlate with the histologic grade and clinical stage of the disease (25,26). However, FdG-PET has played a limited role in prostate cancer diagnosis mainly because of the relatively low differential uptake of FdG in most primary prostate tumors and because the bladder produces a very strong FdG signal near the prostate. Meanwhile, proton nuclear magnetic resonance (NMR) spectroscopic studies performed on extracts of transurethral resection specimens (15) and high-resolution magic angle spinning spectroscopic studies of intact surgical (16) and biopsy (17) samples from human prostate tissue have shown significantly higher levels of lactate in prostate cancer samples than in normal prostate samples. Based on the FdG-PET studies and the spectroscopic

[6]American Cancer Society [homepage on the Internet]. Atlanta (GA): American Cancer Society; c2007 [updated 2007]. Cancer facts and figures 2007. Available from: http://www.cancer.org/docroot/STT/STT_0.asp.

studies, it seems likely that prostate cancer causes or is dependent on an increase in glycolytic rates as has been suggested for other cancers (18). In addition, the spectroscopic studies found higher alanine levels in prostate cancer samples relative to the normal prostate tissue samples. The extra alanine might be a byproduct of lipogenesis because alanine transamination would support the oxidation of glutamate to α-ketoglutarate, which could provide the carbon molecules required for lipogenesis instead of pyruvate/lactate oxidation (27,28) or it may be used directly for protein synthesis. Whatever the biological mechanism may be for the enhanced lactate and alanine production, lactate and alanine levels have yet to be measured noninvasively *in vivo* because the low concentrations of lactate and alanine in prostate tissue make the detection of these metabolites difficult. Furthermore, the need to suppress large fat signals from lipids surrounding the prostate (29) has made it difficult to observe lactate and alanine with *in vivo* ^{1}H MRSI studies as the lipids resonate at frequencies near lactate and alanine. However, new hyperpolarized ^{13}C spectroscopic imaging techniques (30–32) may provide an opportunity to observe the changes in lactate and alanine in a MRI exam of prostate cancer patients.

^{13}C-labeled substrates have recently been polarized using dynamic nuclear polarization (DNP) techniques to obtain tens of thousands fold enhancement of the ^{13}C NMR signals from the substrate as well as its metabolic products (30,33,34). Preliminary DNP studies in rats, rat xenograft tumors, mouse lymphoma tumors, and a transgenic mouse model of prostate cancer have shown >50,000-fold enhancements in the polarization of [1-^{13}C] pyruvate and its metabolic products, providing sufficient MR signal for high spatial and temporal resolution spectroscopic imaging of the metabolites (31,32,35,36). Pyruvate is ideal for these studies because the hyperpolarized MR signal from the C-1 carbon relaxes very slowly as a result of its long T_1 and it is at the entry point to several important energy and biosynthetic pathways. In particular, it is converted to lactate in glycolysis, to alanine for protein synthesis and/or lipogenesis, and to acetyl-CoA and oxaloacetate to support the tricarboxylic acid cycle and biosynthesis of membrane lipids. Based on the published success of DNP and its application to pyruvate (31,32,35), hyperpolarization of [1-^{13}C]pyruvate provides an excellent opportunity to noninvasively measure the lactate and alanine differences that likely exist between the various grades of prostate cancer.

The aim of this study was to quantify the differences in hyperpolarized [1-^{13}C] pyruvate and its metabolic products between the various grades of prostate cancer in the transgenic adenocarcinoma of mouse prostate (TRAMP) model. The TRAMP model is particularly useful for studying the metabolic changes that occur with prostate cancer evolution and progression because TRAMP mice show a histopathologic disease progression (37) and the associated metabolic changes that mimic the human disease. Furthermore, preliminary studies have shown that TRAMP mice tumors exhibited significant lactate and alanine signals following the injection of hyperpolarized [1-^{13}C] pyruvate (32). In the present study, normal mice and TRAMP mice with low- and high-grade primary tumors were injected with hyperpolarized [1-^{13}C] pyruvate and imaged using a custom three-dimensional ^{13}C MRSI technique. The histopathologic findings from the resected tumors were used to grade the tumors and to classify the mice into three groups. The results from this study provided a three-dimensional visualization of the distribution of hyperpolarized pyruvate and its metabolic products throughout the tumors and the surrounding anatomy. The differences in hyperpolarized lactate levels were so distinct that it would have been possible to noninvasively grade the disease in all but one of the mice included in this study.

Materials and Methods

Animal preparation and MR system configuration

All the mice were bred by crossing C57BL6 and FVB mice and were studied under a protocol approved by the University of California San Francisco Institutional Animal Care and Utilization Committee. The four TRAMP mice histologically classified as low-grade mice (21–28 wk old) and the three high-grade TRAMP mice (27–40 wk old) were imaged a total of six and five times, respectively. The five normal mice (17–39 wk old) were imaged a total of seven times. For all the mice, a 28-gauge catheter that extended from the dorsal surface of their neck was surgically implanted into one of their jugular veins at least 1 d before the hyperpolarized MR study. At the time of the MR experiment, the mice were anesthetized with 1% to 1.5% isoflurane and a 90-cm-long, 24-gauge extension tube was connected to the jugular vein port (Strategic Applications). This special extension tube made it possible to quickly inject the hyperpolarized agent into a mouse inside a human MR scanner while maintaining a low dead volume in the tubing. Next, the mice were placed on a water-filled, temperature-controlled pad that was heated to approximately 37°C and positioned inside of custom-built dual-tuned proton-carbon transmit/receive coil. The entire setup was positioned in the bore of a 3T human GE scanner equipped with the multinuclear spectroscopy package (GE Healthcare).

MRI and hyperpolarization studies

All the mice were scanned following a previously published protocol (32). In brief, T_2-weighted ^{1}H anatomic MR images were acquired in sagittal, axial, and coronal views. A mixture of [1-^{13}C] pyruvic acid and the trityl radical {tris(8-carboxy-2,2,6,6,-tetra (methoxyethyl)benzo[1,2-d:4,5-d′]bis(1,3)dithiole-4-yl)methyl sodium salt; GE Healthcare} was polarized to 21.7 ± 2.0% using a prototype polarizer developed by GE Healthcare (30). After the mixture was polarized, it was rapidly dissolved into a pH-balanced Tris buffer solution using previously published techniques (30) and yielded a hyperpolarized 79 mmol/L pyruvate solution with a pH of 7.9 ± 0.2 (31,32). Next, the solution was quickly transported to the MR scanner and 350 ± 50 μL (28 μmol pyruvate) of it were injected into the mouse during a 12-s interval, resulting in a blood concentration of ~ 9 mmol/L pyruvate. The hyperpolarized pyruvate was immediately cleared from the injection tubing using a 150 μL saline flush. For the hyperpolarized dynamic study, a ^{13}C spectrum was acquired every 3 s from a 10-mm-thick slab centered on the primary tumor in a high-grade TRAMP mouse. The spectra were recorded using a 5° excitation pulse, 2,048 points, and a 5 kHz bandwidth. For the hyperpolarized MRSI studies, a double spin-echo pulse sequence with a small variable flip-angle excitation pulse, adiabatic refocusing pulses, and a flyback echo-planar readout trajectory was used to acquire *in vivo* three-dimensional ^{13}C MRSI data in 14 s (38). Based on the time course in Fig. 1, the imaging data acquisition was initiated 35 s after the start of the pyruvate injection because the hyperpolarized lactate signal was relatively constant from 35 to 49 s. Three-dimensional MRSI data were acquired from the abdomen of the mice using a echo time/repetition time of 140/215 ms, an 8 × 8 × 16 matrix, a 40 × 40 × 86.4 mm field of view (0.135 cm^3 spatial resolution), 59 points per spectrum, and a 581 Hz bandwidth.

Histopathologic analysis

The pathology was correlated with the anatomic images by displaying the sagittal, coronal, and axial images of the TRAMP mice on a laptop computer during the dissection using OsiriX (Open Source). Additionally, digital photographs and videos were taken during the dissection and subsequently reviewed. The excised tissues were immediately fixed in 10% buffered formalin, subsequently transitioned into ethanol, and embedded in paraffin blocks. Tissue blocks were cut into 5-μm-thick sections on a Leica microtome. Sections were dried onto glass slides and stained using a standard H&E protocol. The percentage of normal, well-differentiated, moderately well-differentiated, and poorly differentiated tissue was estimated

from microscopic examination as previously published (39) and was used to classify the primary tumors into low-and high-grade categories (Table 1). The percentage of necrosis was also estimated for the low-grade tumors and lymph node metastases (Table 1). Using these percentages, a histology index was determined for each of the tumors by assigning the normal, well-differentiated, moderately well-differentiated, and poorly differentiated tissue with a value of 0, 1, 2, and 3, respectively. The index was computed by multiplying the volume percentages by these values and summing the weighted percentages. For tumors smaller than 0.2 cm^3 (volume of cylinder containing a 0.135 cm^3 square cuboid), the percentages were adjusted to represent a 0.2 cm^3 volume for the index calculation by assuming that the nontumor tissue in this volume was normal.

Data processing

The primary and metastatic regions of prostate cancer identified during dissection were traced on the corresponding anatomic images using custom software that reported the volumes for the traced regions. For the hyperpolarized dynamic study, the peak height of pyruvate, lactate, and alanine was measured in the ^{13}C spectrum at each time point, after the spectrum was apodized with a 11.4 Hz Gaussian filter. The metabolite peak heights were then corrected for the magnetization used to acquire the previous time points and plotted as a function of time. For the hyperpolarized carbon imaging studies, the MRSI data were spatially zero filled to a 16 × 16 × 32 matrix, spectrally apodized with a 10 Hz Gaussian filter, frequency referenced to [1-^{13}C] lactate,[7] and aligned with anatomic images using custom software. Because the metabolite peak area is proportional to the amount of the metabolite present in the voxel, all of the spectroscopic voxels were integrated over a predetermined frequency range for each of the metabolites. Images of the lactate integrals were created by spatially interpolating the lactate data to the resolution of the anatomic images using a sinc kernel and overlaying the lactate image onto the anatomic image with 60% opacity.

Data analysis

For each study, the integrals for a given metabolite from voxels containing the same tissue type were scaled by the noise calculated from a region of the spectrum that did not contain any metabolites and were averaged together to produce peak area signal-to-noise ratios (SNR). The sum of the lactate, alanine, and pyruvate integrals, labeled total hyperpolarized carbon (THC), was computed and used as an estimate of the amount of hyperpolarized compounds taken up by the tissue. Using Statistical Analysis System (SAS), an ANOVA was computed for each metabolite and for THC, along with pairwise *t* tests across the four groups that were corrected for multiple comparisons with the Tukey correction. A random effects model was incorporated into the statistical tests to correct for any correlation that may have been caused by including multiple studies from the same animal (40). Next, the saturation of the conversion of the hyperpolarized compounds to lactate was evaluated for each tissue type by fitting the lactate versus THC data with a linear function and comparing the slope with one. A slope of one would indicate complete conversion to lactate (lactate = THC). Last of all, a correlation coefficient was computed for the histologic index and the lactate levels in Table 1 as well as the lactate levels in Fig. 5.

Results

The hyperpolarization of [1-^{13}C] pyruvate provided ample signal to noise for measuring the time course of the delivery of the labeled pyruvate as well as its metabolic conversion to lactate

[7]Department of Biochemistry. Biological Magnetic Resonance Data Bank [database on the Internet]. Madison (WI): University of Wisconsin. c2007 [updated 2007 Feb 28; cited 2007 May 1]. Available from: http://www.bmrb.wisc.edu/metabolomics/metabolomics_standards.html.

and alanine in a 10-mm-thick slab from an anaesthetized TRAMP mouse as shown in Fig. 1. The hyperpolarized pyruvate (173 ppm) was detected in the slab ~ 12 s after the start of the injection and reached its maximum level ~ 12 s later, as expected from a 12-s-long injection of pyruvate. Hyperpolarized [1-^{13}C] lactate (185 ppm) was observed in the axial slab from the mouse almost immediately following the arrival of the labeled pyruvate and increased in concentration at a slightly slower rate than the labeled pyruvate. Because the labeled lactate was reduced from the labeled pyruvate by lactate dehydrogenase (LDH), the signal from the hyperpolarized pyruvate rapidly decreased from its maximum until the lactate and pyruvate approached isotopic equilibrium at ~ 45 s. At this point, both lactate and pyruvate decreased at a slower rate as result of T_1 relaxation, use of the hyperpolarized signal for the MR experiment, and metabolic conversation to other compounds. The slow decrease allowed the labeled lactate signal to persist for over 2 min. Hyperpolarized [1-^{13}C] alanine (178.5 ppm) was also observed in the slab through the TRAMP tumor and exhibited a behavior analogous to lactate, except that the conversion from pyruvate to alanine was controlled by alanine transaminase and the amount of hyperpolarized alanine produced was an order of magnitude lower than that of lactate. The pyruvate hydrate (181 ppm) present in the spectra followed the same time course as pyruvate because it was in equilibrium with the pyruvate. However, it had a substantially lower signal level. For this study, the time course data were used to define the timing of the spectroscopic imaging experiments.

Out of the seven TRAMP mice included in the hyperpolarized imaging experiments, three were histologically classified with high-grade tumors and four were classified with low-grade tumors. The TRAMP mice with high-grade tumors had very large primary tumors and periaortic lymph node metastases that were 6.9 ± 4.8 cm^3 and 0.41 ± 0.50 cm^3, respectively. As indicated in Table 1, the high-grade tumors were almost exclusively poorly differentiated cells with a histologic index between 2.4 and 2.8. The lymph node metastases were mostly poorly differentiated cells along with some necrosis and had a histologic index between 1.4 and 2.3. A representative TRAMP mouse with a high-grade 4.3 cm^3 tumor and a right periaortic lymph node metastasis is shown in axial cross-section in the anatomic image in Fig. 2*A*. The spatially interpolated hyperpolarized lactate image from this mouse presented in Fig. 2*B* shows a very strong lactate signal (165 ± 34) from the active region of the primary tumor and a moderately strong lactate signal (104 ± 6.5) from the lymph node metastasis. The remaining tissue, including the necrotic regions in the anterior aspect of the tumor, yielded orders of magnitude lower lactate. The grid of ^{13}C spectra taken from the three-dimensional MRSI shows a high lactate-to-pyruvate ratio across the tumor (2.2 ± 0.48) and in the lymph node metastasis (2.0 ± 0.03) along with low alanine levels relative to pyruvate. All the metabolite levels in the spectra located outside of the tumors were substantially lower.

The low-grade tumors were 0.23 ± 0.10 cm^3 and were composed of well-differentiated, moderately well-differentiated, and poorly differentiated tumor tissue along with a few normal epithelial areas (Table 1). These tumors had histologic indices ranging from 0.7 to 1.9. As illustrated by the representative case in Fig. 3*A* and *B*, the low-grade tumors were clearly visualized on the anatomic images and exhibited higher hyperpolarized lactate levels (SNR = 75) than the surrounding tissue. The carbon spectrum taken from the three-dimensional MRSI shows that the hyperpolarized lactate and pyruvate levels were comparable in the low-grade tumors, whereas the alanine level was again much lower.

After comparing the hyperpolarized lactate levels with the histologic index determined from the H&E-stained sections, the lactate levels and histologic index had a correlation coefficient of 0.95 when using the average lactate values in Table 1 and 0.92 when using the individual lactate values in Fig. 5. The representative hyperpolarized carbon spectra and H&E-stained sections from each of histologically defined groups shown in Fig. 4 illustrate this strong correlation. The hyperpolarized spectrum from the normal murine prostate exhibited the lowest

lactate level out of all the representative spectra, whereas pyruvate produced the largest peak in the normal spectrum. As a side note, the normal prostate spectra also included metabolic signals from surrounding tissues because the spectroscopic voxel was larger than the normal mouse prostate. Similar to the healthy human prostate, the murine prostate histology was very glandular with secretory epithelial cells lining the glands and stromal tissue supporting the glands as shown in Fig. 4*A*. The histologic sections from the low- and high-grade tumors depict the gradual replacement of the secretory epithelial cells by less differentiated epithelial cells until the glands were completely eliminated and only anaplastic sheets of pleomorphic cells with irregular nuclei remained in the high-grade tumors. The carbon spectra showed significantly higher hyperpolarized lactate levels in the primary tumors, with the high-grade tumors having the highest lactate levels. Pyruvate levels in the primary tumors were similar and were comparable with the normal prostates and lymph node metastases (Fig. 4). Lactate levels in the lymph node metastases fell between those of the primary tumors. Histologically, the lymphocytes in the lymph nodes were almost completely replaced by poorly differentiated epithelial cells.

Evaluating all of the samples collectively, statistical comparisons revealed that the lactate levels between all the groups were different with the exception that low-grade tumors were not different from lymph node metastases ($P < 0.05$). Very importantly, there was almost no overlap between the normal prostates, low-grade tumors, and high-grade tumors, an essential characteristic of an accurate grading tool. In fact, the lactate levels from six of the seven normal prostates were lower than the lactate levels measured in all the tumors as shown in Fig. 5. Using the THC as a rough measure of uptake of the hyperpolarized substrates, it was clear that the seventh normal mouse prostate also received much more hyperpolarized carbon. Despite the higher uptake, the lactate levels were only slightly higher, indicating that a small amount of additional hyperpolarized carbons present in the prostate had been converted to lactate, whereas the high-grade tumors had much higher THC relative to the normal prostates and much higher hyperpolarized lactate. As a rough measure of the conversion to lactate, the lactate versus THC data for the groups plotted in Fig. 5*D* were fit with linear functions. The slopes of the lines were 0.27, 0.41, and 0.53 for the normal prostates, low-grade tumors, and high-grade tumors, respectively. Because the slope increased with grade, it suggests that the ability to convert pyruvate to lactate increased with the grade of the tumor or the demand for converted lactate increased with grade. Furthermore, the increase in THC with grade indicates that the uptake of the hyperpolarized compounds increased with grade as well. Statistically, THC levels in the high-grade tumors were different from all of the other groups ($P < 0.05$). The difference in THC levels between low-grade tumors and normal prostates was approaching statistical significance with $P = 0.08$. Meanwhile, hyperpolarized alanine levels were only marginally different from a statistical standpoint with the comparison between high-grade tumors and normal prostates yielding $P = 0.05$. Nonetheless, alanine levels exhibited trends that were similar to the trends in lactate levels but with smaller differences and SDs as shown in Fig. 5. The individual hyperpolarized pyruvate values had significant overlap between the groups (plot not shown) and were not statistically different across the groups.

Discussion

The data from this study show that hyperpolarized [1-^{13}C] lactate levels measured after the injection of hyperpolarized [1-^{13}C] pyruvate provide a noninvasive measure of the histologic grade of prostate cancer in TRAMP mice. Not only were the lactate levels grade dependent, the lactate levels in the tumor were higher than those from the surrounding anatomy, indicating that hyperpolarized lactate has the potential to be a very sensitive biomarker for prostate cancer localization and detection. In addition, the overlap between the normal prostates, low-grade tumors, and high-grade tumors was minimal with just one normal prostate having a lactate level that overlapped with the low-grade tumors.

The hyperpolarized lactate levels were strongly correlated with the histologic index (0.95) of the cancer, which was determined from the amount of well, moderately well, and poorly differentiated epithelial tissue present in the tumor. Because the same histologic data were used to determine the histologic grade, the hyperpolarized lactate levels also correlated with the grade of the tumor. Low-grade tumors contained a significant percentage of well-differentiated epithelium and produced tumors that were slightly larger than the normal murine prostate. High-grade tumors consisted of mostly poorly differentiated epithelium and coexisted with significant lymph node metastases. The disease progression in the TRAMP mice included in this study was consistent with a previous study, which showed that the TRAMP transgene causes the glandular architecture of the murine prostate to gradually be replaced by less differentiated epithelial cells, resulting in primary tumors that are almost entirely poorly differentiated cells in the advanced stages of the disease (39). In addition, the investigators showed that as the primary tumors progressed, the TRAMP mice also develop metastases that first appeared in the regional lymph nodes.

The higher lactate levels found in the tumors in the present study are consistent with lactate measurements made on human prostate tissue samples (15–17) as well as hyperpolarized lactate measurements made in rat tumor xenografts (35) and mouse lymphoma tumors (36). These findings support the hypothesis that the cellular evolution associated with carcinogenesis selects for lactate-producing glycolytic cells because they can withstand the intermittent hypoxia that malignant cells likely endure and it supports the microenvironmental acidosis they need to breakdown and invade the surrounding healthy tissues (18,24). Additionally, the larger lactate pool may be a carbon source for the lipogenesis that is required to sustain cellular proliferation (19). Because LDH is the only known mechanism for converting pyruvate to lactate, the higher hyperpolarized lactate levels reported in this study are likely a reflection of higher LDH activity within the region of interest. The *in vivo* LDH activity may have been influenced by the amount of pyruvate delivered to the cells and the concentrations of LDH and its cofactors. Because THC levels and the slope of the lactate versus THC data increased with tumor grade, it seems that more pyruvate was delivered to the cells because of increased transporter expression and/or blood perfusion and the cells contained more active LDH and/or cofactors. Although it is possible that the pyruvate to lactate conversion occurred before its delivery to the tumor tissue, the fact that the pyruvate signal buildup preceded the lactate signal buildup in the time course data suggests that the pyruvate was delivered to the tumor tissue. In addition, the hyperpolarized lactate-to-pyruvate ratio was found to be much less than one in the blood of rats with tumor xenografts (35) and the blood of mice with lymphoma tumors (36) that were examined using a similar hyperpolarized imaging protocol. Naturally, these assertions need to be verified in future TRAMP mice studies by directly measuring the LDH activity levels in the tumors and by developing a hyperpolarized imaging technique capable of measuring the time course of the hyperpolarized metabolites in smaller regions of interest.

Differences in hyperpolarized alanine and pyruvate were not as substantial as the changes in lactate across the various tumor types. Although the differences were much smaller for alanine, it did show a trend for the same grade-dependent changes observed for lactate. A study performed on isolated mitochondria showed that tumor cell mitochondria produced alanine in the presence of pyruvate to support the conversion of glutamate to citrate, which would enable the biosynthesis of new cell membranes (27). These findings along with the elevated alanine levels measured in human prostate cancer samples (15–17) suggest that the hyperpolarized alanine differences from this study are real and would have reached statistical significance with a larger sample size. The pyruvate levels were more variable than the lactate and alanine levels and gave no indication of a difference between the groups. Because the hyperpolarized pyruvate signal was rapidly decreasing while the ^{13}C MRSI data were being recorded (Fig. 1), the large variability was likely caused by the timing of the data acquisition. If one assumes that most of the lactate and alanine were converted from the pyruvate after it arrived in the tissue of interest,

then the THC levels provide a good estimate of the amount of pyruvate taken up by the tissue. As it turned out, the THC levels increased with the grade of the cancer and suggest that the amount of pyruvate uptake was grade dependent as well. The higher pyruvate uptake in cancer is consistent with a cellular study that showed that a monocarboxylate transporter (MCT-2) had high affinity for pyruvate and had higher mRNA expression in epithelial tumor cell lines (41). Although the THC levels increased with grade, there was slightly more overlap in the individual THC levels between grades compared with the lactate levels. However, the THC levels helped explain the variation in lactate levels within each tumor type.

In the clinic, the detailed information obtained from the spectroscopic imaging of hyperpolarized pyruvate and its metabolic products may improve prostate cancer patient care by providing a method to noninvasively characterize cancer throughout the entire prostate with a single procedure. The hyperpolarized MRSI procedures presented here allowed three-dimensional visualization of the distribution of lactate, pyruvate, and alanine throughout the prostate tumor and surrounding anatomy. With this technique, it was possible to noninvasively detect low-grade tumors as well as regional lymph node metastases. As part of current clinical practice, TRUS-guided pattern biopsies, a more invasive approach, are used to diagnose prostate cancer, but the procedures are limited by the ability of TRUS to locate the tumor and the small percentage of the prostate that is sampled. Clearly, a more comprehensive noninvasive measurement would be superior. In addition, the strong correlation between the hyperpolarized lactate levels and the grade of the tumor, along with the minimal overlap in lactate levels between different grades, suggests that physicians could use the information to choose the best therapy and treatment schedule for an individual patient or improve TRUS-guided biopsy planning. For the murine studies presented here, the THC levels did not improve the accuracy of the tumor grading. However, the combination of lactate levels and THC levels may prove even more beneficial than lactate alone for *in vivo* human exams. From a biological standpoint, the highly reproducible difference in the hyperpolarized lactate levels suggests that the hyperpolarization assay augmented with the appropriate experimental conditions may provide a noninvasive technique for monitoring changes in LDH activity.

In summary, the grade dependence of hyperpolarized lactate levels was measured for the first time in a transgenic mouse model of prostate cancer. The amount of hyperpolarized lactate measured after injection of hyperpolarized ^{13}C pyruvate showed great potential as a new biomarker capable of noninvasively grading prostate cancer in mice and great potential for future studies of prostate cancer patients. The amount of THC was also grade dependent, but the THC levels in individual tumors produced slightly more overlap between the different tumor grades than the individual lactate levels. However, the THC explained some of the within-group variation in hyperpolarized lactate, suggesting that a combination of these biomarkers will likely provide the best characterization of prostate cancer aggressiveness in patients.

Acknowledgments

Grant support: NIH grant R21EB05363 and University of California Discovery grants LSIT01-10107 and ITL-BIO04-10148.

We thank Ying Lu and Helena Gurascier for their assistance with the statistical analysis; Jason Crane for developing the software used to create the metabolic images; Lucas Carvajal and Paul Calderon for assisting with the RF coil fabrication and maintenance; David Joun for sectioning and staining the histology slides; Norm Greenberg and Barbara Foster for providing several of the TRAMP mice used in these studies; and Jan-Henrik Ardenkjaer-Larsen, Jan Wolber, and Jonathan Murray from GE Healthcare for transferring the DNP technology to University of California San Francisco and for supporting it.

References

1. Carroll PR. Early stage prostate cancer—do we have a problem with over-detection, overtreatment or both? J Urol 2005;173:1061–2. [PubMed: 15758699]
2. McNeal JE, Bostwick DG, Kindrachuk RA, Redwine EA, Freiha FS, Stamey TA. Patterns of progression in prostate cancer. Lancet 1986;1:60–3. [PubMed: 2867314]
3. Stamey TA. Cancer of the prostate: an analysis of some important contributions and dilemmas. Mono Urol 1982;3:67–94.
4. Kurhanewicz J, Vigneron DB, Hricak H, Narayan P, Carroll P, Nelson SJ. Three-dimensional H-1 MR spectroscopic imaging of the *in situ* human prostate with high (0.24–0.7-cm3) spatial resolution. Radiology 1996;198:795–805. [PubMed: 8628874]
5. Hasumi M, Suzuki K, Taketomi A, et al. The combination of multi-voxel MR spectroscopy with MR imaging improve the diagnostic accuracy for localization of prostate cancer. Anticancer Res 2003;23:4223–7. [PubMed: 14666629]
6. Portalez D, Malavaud B, Herigault G, et al. Predicting prostate cancer with dynamic endorectal coil MR and proton spectroscopic MR imaging. J Radiol 2004;85:1999–2004. [PubMed: 15692410]
7. Scheidler J, Hricak H, Vigneron DB, et al. Prostate cancer: localization with three-dimensional proton MR spectroscopic imaging—clinicopathologic study. Radiology 1999;213:473–80. [PubMed: 10551229]
8. Squillaci E, Manenti G, Mancino S, et al. MR spectroscopy of prostate cancer. Initial clinical experience. J Exp Clin Cancer Res 2005;24:523–30. [PubMed: 16471314]
9. Vilanova JC, Barcelo J. Prostate cancer detection: magnetic resonance (MR) spectroscopic imaging. Abdom Imaging 2007;32:253–61. [PubMed: 17476554]
10. Wefer AE, Hricak H, Vigneron DB, et al. Sextant localization of prostate cancer: comparison of sextant biopsy, magnetic resonance imaging and magnetic resonance spectroscopic imaging with step section histology. J Urol 2000;164:400–4. [PubMed: 10893595]
11. Yu KK, Scheidler J, Hricak H, et al. Prostate cancer: prediction of extracapsular extension with endorectal MR imaging and three-dimensional proton MR spectroscopic imaging. Radiology 1999;213:481–8. [PubMed: 10551230]
12. Wang L, Hricak H, Kattan MW, Chen HN, Scardino PT, Kuroiwa K. Prediction of organ-confined prostate cancer: incremental value of MR imaging and MR spectroscopic imaging to staging nomograms. Radiology 2006;238:597–603. [PubMed: 16344335]
13. Kurhanewicz J, Vigneron DB, Males RG, Swanson MG, Yu KK, Hricak H. The prostate: MR imaging and spectroscopy. Present and future. Radiol Clin North Am 2000;38:115–38. [PubMed: 10664669]
14. Zakian KL, Sircar K, Hricak H, et al. Correlation of proton MR spectroscopic imaging with gleason score based on step-section pathologic analysis after radical prostatectomy. Radiology 2005;234:804–14. [PubMed: 15734935]
15. Cornel EB, Smits GA, Oosterhof GO, et al. Characterization of human prostate cancer, benign prostatic hyperplasia and normal prostate by *in vitro* ^{1}H and ^{31}P magnetic resonance spectroscopy. J Urol 1993;150:2019–24. [PubMed: 7693985]
16. Swanson MG, Zektzer AS, Tabatabai ZL, et al. Quantitative analysis of prostate metabolites using ^{1}H HR-MAS spectroscopy. Magn Reson Med 2006;55:1257–64. [PubMed: 16685733]
17. Tessem MB, Swanson MG, Keshari KR, et al. Evaluation of lactate and alanine as metabolic biomarkers of prostate cancer using ^{1}H HR-MAS; spectroscopy of biopsy tissues. Magn Reson Med 2008;60:510–6. [PubMed: 18727052]
18. Gatenby RA, Gillies RJ. Why do cancers have high aerobic glycolysis? Nat Rev Cancer 2004;4:891–9. [PubMed: 15516961]
19. Costello LC, Franklin RB. 'Why do tumour cells glycolyse?': from glycolysis through citrate to lipogenesis. Mol Cell Biochem 2005;280:1–8. [PubMed: 16511951]
20. Mochiki E, Kuwano H, Katoh H, Asao T, Oriuchi N, Endo K. Evaluation of ^{18}F-2-deoxy-2-fluoro-D-glucose positron emission tomography for gastric cancer. World J Surg 2004;28:247–53. [PubMed: 14961197]

21. Kunkel M, Reichert TE, Benz P, et al. Overexpression of Glut-1 and increased glucose metabolism in tumors are associated with a poor prognosis in patients with oral squamous cell carcinoma. Cancer 2003;97:1015–24. [PubMed: 12569601]
22. Warburg O, Wind F, Negelein E. Uber den Stoffwechsel von Tumouren im Korper. Klin Woch 1926;5:829–32.
23. Warburg O. On the origin of cancer cells. Science 1956;123:309–14. [PubMed: 13298683]
24. Gatenby RA, Gawlinski ET, Gmitro AF, Kaylor B, Gillies RJ. Acid-mediated tumor invasion: a multidisciplinary study. Cancer Res 2006;66:5216–23. [PubMed: 16707446]
25. Oyama N, Akino H, Kanamaru H, Okada K. Fluorodeoxyglucose positron emission tomography in diagnosis of untreated prostate cancer. Nippon Rinsho 1998;56:2052–5. [PubMed: 9750506]
26. Kanamaru H, Oyama N, Akino H, Okada K. Evaluation of prostate cancer using FDG-PET. Hinyokika Kiyo 2000;46:851–3. [PubMed: 11193311]
27. Moreadith RW, Lehninger AL. The pathways of glutamate and glutamine oxidation by tumor cell mitochondria. Role of mitochondrial NAD(P)$^+$-dependent malic enzyme. J Biol Chem 1984;259:6215–21. [PubMed: 6144677]
28. DeBerardinis RJ, Mancuso A, Daikhin E, et al. Beyond aerobic glycolysis: transformed cells can engage in glutamine metabolism that exceeds the requirement for protein and nucleotide synthesis. Proc Natl Acad Sci U S A 2007;104:19345–50. [PubMed: 18032601]
29. Nelson SJ, Vigneron DB, Star-Lack J, Kurhanewicz J. High spatial resolution and speed in MRSI. NMR Biomed 1997;10:411–22. [PubMed: 9542738]
30. Ardenkjaer-Larsen JH, Fridlund B, Gram A, et al. Increase in signal-to-noise ratio of >10,000 times in liquid-state NMR. Proc Natl Acad Sci U S A 2003;100:10158–63. [PubMed: 12930897]
31. Kohler SJ, Yen Y, Wolber J, et al. *In vivo* (13)carbon metabolic imaging at 3T with hyperpolarized (13)C-1-pyruvate. Magn Reson Med 2007;58:65–9. [PubMed: 17659629]
32. Chen AP, Albers MJ, Cunningham CH, et al. Hyperpolarized C-13 spectroscopic imaging of the TRAMP mouse at 3T-initial experience. Magn Reson Med 2007;58:1099–106. [PubMed: 17969006]
33. Golman K, Olsson LE, Axelsson O, Mansson S, Karlsson M, Petersson JS. Molecular imaging using hyperpolarized ^{13}C. Br J Radiol 2003;76:S118–27. [PubMed: 15572334]
34. Mansson S, Johansson E, Magnusson P, et al. ^{13}C imaging—a new diagnostic platform. Eur Radiol 2006;16:57–67. [PubMed: 16402256]
35. Golman K, Zandt RI, Lerche M, Pehrson R, Ardenkjaer-Larsen JH. Metabolic imaging by hyperpolarized ^{13}C magnetic resonance imaging for *in vivo* tumor diagnosis. Cancer Res 2006;66:10855–60. [PubMed: 17108122]
36. Day SE, Kettunen MI, Gallagher FA, et al. Detecting tumor response to treatment using hyperpolarized (13)C magnetic resonance imaging and spectroscopy. Nat Med 2007;13:1382–7. [PubMed: 17965722]
37. Greenberg NM, DeMayo F, Finegold MJ, et al. Prostate cancer in a transgenic mouse. Proc Natl Acad Sci U S A 1995;92:3439–43. [PubMed: 7724580]
38. Cunningham CH, Chen AP, Albers MJ, et al. Double spin-echo sequence for rapid spectroscopic imaging of hyperpolarized (13)C. J Magn Reson 2007;187:357–62. [PubMed: 17562376]
39. Gingrich JR, Barrios RJ, Foster BA, Greenberg NM. Pathologic progression of autochthonous prostate cancer in the TRAMP model. Prostate Cancer Prostatic Dis 1999;2:70–5. [PubMed: 12496841]
40. Diggle, PJ.; Liang, K-Y.; Zeger, SL. Parametric models for covariance structure. New York: Oxford University Press; 1994. p. 78-116.
41. Lin RY, Vera JC, Chaganti RS, Golde DW. Human monocarboxylate transporter 2 (MCT2) is a high affinity pyruvate transporter. J Biol Chem 1998;273:28959–65. [PubMed: 9786900]

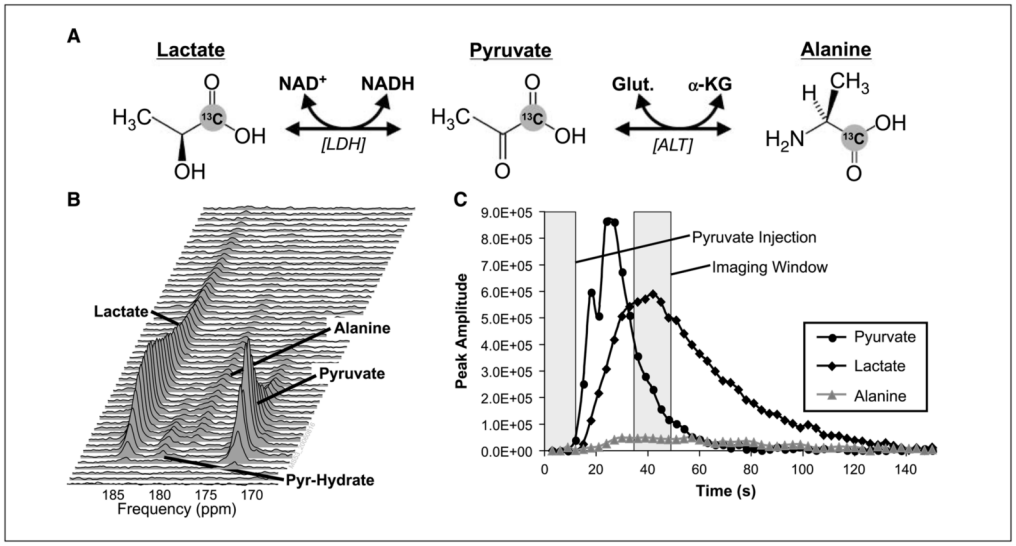

Figure 1.

A, diagram of the [1-^{13}C] pyruvate and the metabolic pathways relevant to this study. The hyperpolarized ^{13}C spectra (*B*) and peak height plots (*C*) show the time course for the hyperpolarized [1-^{13}C] pyruvate and its metabolic products following the injection of 350 μL of hyperpolarized pyruvate. The pyruvate was injected at a constant rate from 0 to 12 s. The MR spectra were acquired every 3 s from a 28-wk-old TRAMP mouse with a high-grade primary tumor using a 5° flip angle and a 10-mm-thick slice. The peak height plot was corrected for the amount of magnetization used to record the previous n spectra by dividing each peak height by $\cos^n(5°)$. The hyperpolarized pyruvate quickly reached a maximum at 24 s before being converted to lactate and alanine. Based on this time course, the subsequent MRSI data were recorded between 35 and 49 s, a time when the hyperpolarized lactate signal was roughly constant. *Glut.*, glutamate; *α-KG*, α-ketoglutarate; *ALT*, alanine transaminase.

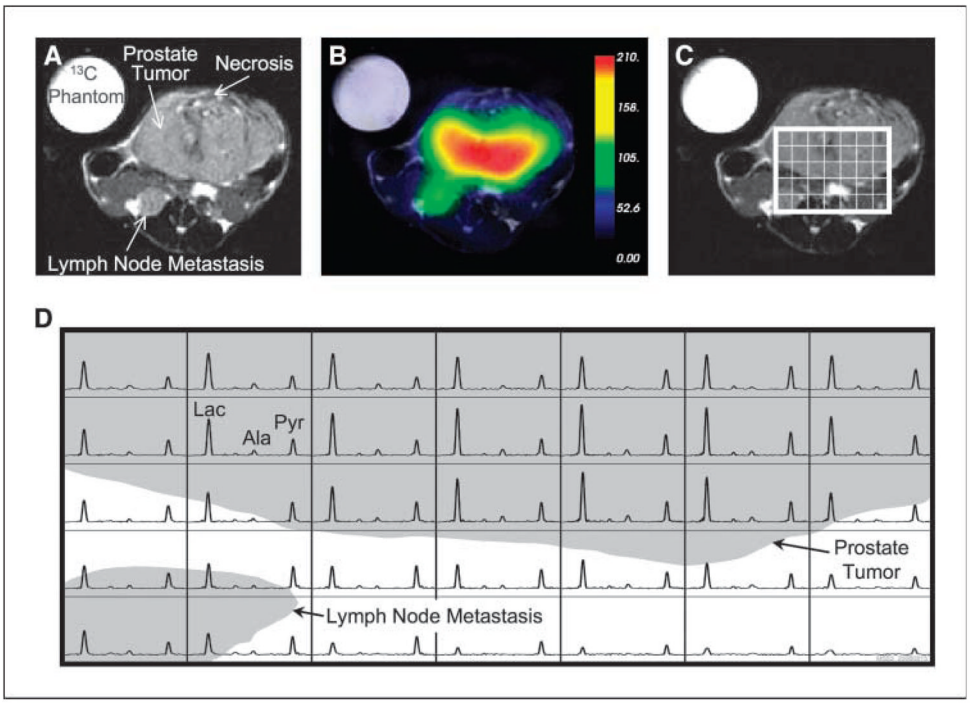

Figure 2.

Axial T_2-weighted ^{1}H image depicting the primary tumor and lymph node metastasis from a TRAMP mouse with a high-grade primary tumor (*A*) and the overlay of an interpolated hyperpolarized ^{13}C lactate image following the injection of 350 μL of hyperpolarized [1-^{13}C] pyruvate (*B*). After spatially zero filling and voxel shifting the ^{13}C spectra to maximize the amount of tumor in the voxels, a subset of the spectral grid was selected (*C*) and displayed (*D*). The three-dimensional MRSI was acquired with a nominal voxel resolution of 135 mm^3 and zero filled to a resolution of 17 mm^3. The spectra show substantially elevated lactate in the high-grade primary tumor compared with the low-grade tumor shown in Fig. 3. In addition, the metabolite signal is significantly lower in the necrotic regions of the primary tumor. *Lac*, lactate; *Ala*, alanine; *Pyr*, pyruvate.

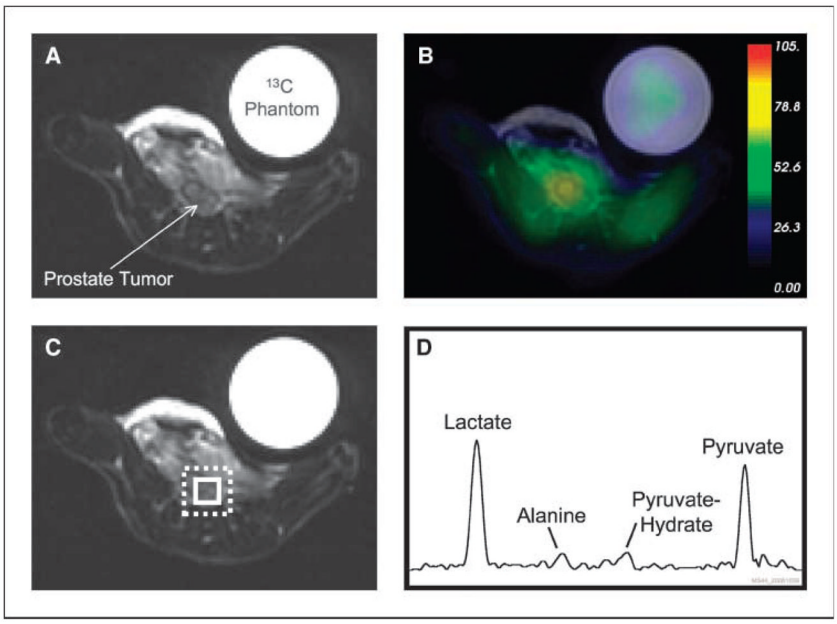

Figure 3.

Axial T_2-weighted ^{1}H image depicting the primary tumor from a TRAMP mouse with a low-grade primary tumor (*A*) and the overlay of an interpolated hyperpolarized ^{13}C lactate image following the injection of 350 μL of hyperpolarized [1-^{13}C] pyruvate (*B*). The numerical range of the color map in the lactate image was reduced to half the range used in Fig. 2 to allow visualization of the lower hyperpolarized lactate levels. After spatially zero filling and voxel shifting the ^{13}C spectra to maximize the amount of tumor in the voxels, one voxel from the primary tumor was selected (*C*) and displayed (*D*). The three-dimensional MRSI was acquired with a nominal voxel resolution of 135 mm^3 (*dashed white box*) and zero filled to a resolution of 17 mm^3 (*solid white box*). The spectrum shows prominent signals from lactate and pyruvate and smaller signals from alanine and pyruvate hydrate.

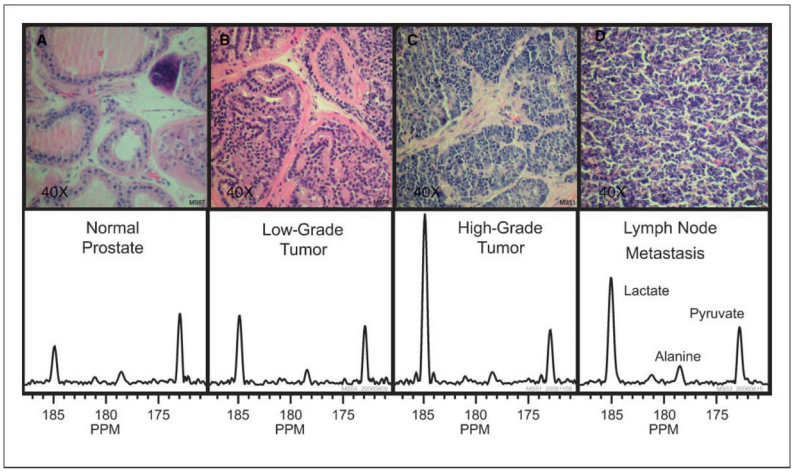

Figure 4.

A to *D*, representative H&E-stained sections and hyperpolarized ^{13}C spectra for one case from each of the histologically defined groups. The histology slides were processed using 5-μm-thick sections and photographed with × 40 magnification. The hyperpolarized ^{13}C spectra represent voxels taken from MRSI data sets and normalized to correct for differences in polarization and receiver sensitivity. The normalized spectra illustrate the strong correlation that exists between the amount of hyperpolarized ^{13}C lactate and the progression of the disease from the normal prostates to the low-grade primary tumors and the high-grade primary tumors.

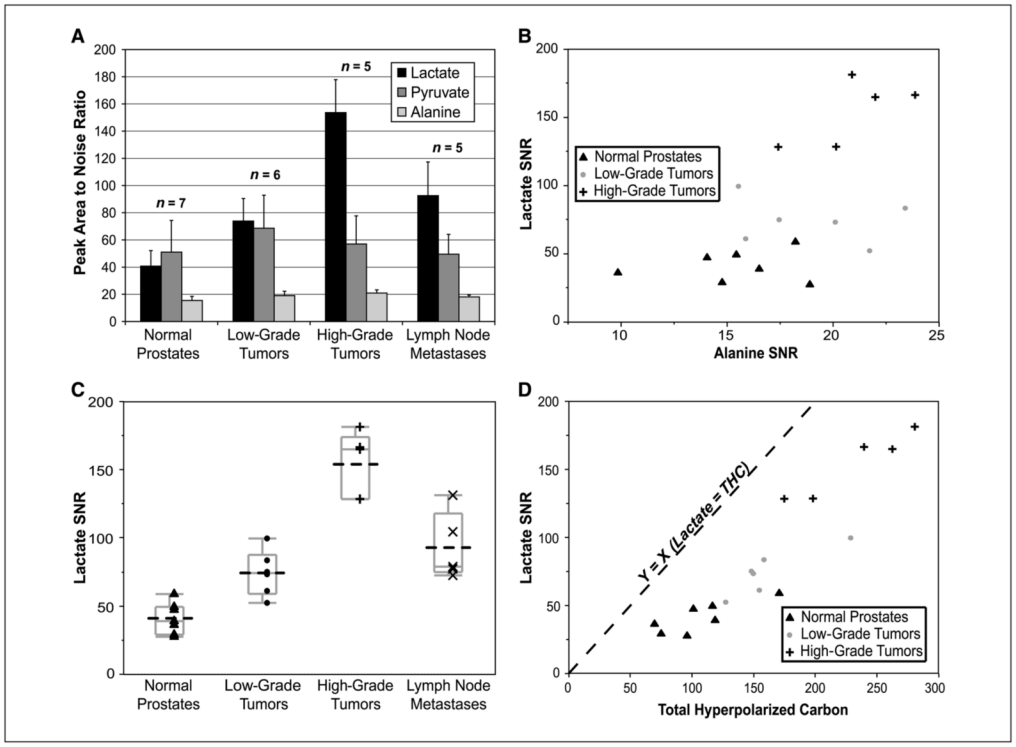

Figure 5.

Numerical comparisons of hyperpolarized ^{13}C metabolites with the pathologically defined groups. Bar plot summarizes the peak area-to-noise ratios of the ^{13}C-labeled lactate, pyruvate, and alanine for the four histologically defined groups (*A*). *Columns,* average; *bars,* SD. The lactate peak area SNR values were statistically different for all four groups, except that low-grade tumors were not different from lymph node metastases ($P < 0.05$). Although the alanine SNR values were not quite statistically different, they exhibited similar trends to the lactate values as shown by the lactate versus alanine plot (*B*). The box plot of the individual values for the lactate SNR (*C*) shows that there was almost no overlap between the normal prostates, low-grade tumors, and high-grade tumors. The plot of lactate versus THC (*D*) suggests that much of the within-group scatter of the lactate SNR may be related to variability in the amount of hyperpolarized carbon delivered to the tissue. All the data presented in these plots were obtained from five normal mice, four TRAMP mice with low-grade primary tumors, and three TRAMP mice with high-grade primary tumors.

Table 1

Histologic classification and average hyperpolarized ^{13}C metabolite SNR for each mouse

Mouse	Gross tissue designation	Histologic classification (%)						Volume (cm^3)	Average metabolite SNR		
		Normal	WD	MWD	PD	Necrotic	Index*		Lactate	Alanine	Pyruvate
MS46	Normal	100†	0	0	0	0	0	0.068	29	15	32
MS47	Normal	100†	0	0	0	0	0	0.051	36	10	24
MS43	Normal	100†	0	0	0	0	0	0.038	39	17	64
MS45	Normal	100†	0	0	0	0	0	0.058	43	19	72
MS67	Normal	100†	0	0	0	0	0	0.043	48	15	46
MS44	LG tumor	1	94	5	0	0	0.74	0.14	63	20	55
MS72	LG tumor	15	78	7	0	0	0.92	0.35	61	16	78
MS36	LG tumor	1	33	1	65	0	1.76	0.15	83	23	52
MS54	LG tumor	2	35	35	30	0	1.95	0.26	86	18	86
MS61	HG tumor	0	0	0	81‡	19§	2.43	12.4	128	17	30
MS51	HG tumor	0	0	1‡	88‡	11§	2.66	4.0	147	22	50
MS53	HG tumor	0	0	0	94.5‡	5.5§	2.84	4.3	173	21	78
MS51	LN metastasis	1	0	0	64	35	1.40	0.14	75	17	48
MS53	LN metastasis	2	0	0	93	5	1.45	0.10	91	19	60
MS61	LN metastasis	4	0	0	76	20	2.28	0.99	131	19	31

Abbreviations: LG, low grade; HG, high grade; LN, lymph node; WD, well differentiated; MWD, moderately well differentiated; PD, poorly differentiated.

*The histologic index ranges between 0 and 3, where 0 indicates that 100% of the tissue was normal and 3 indicates that 100% of the tissue was poorly differentiated. The values for the small tumors were corrected for partial volume effects.

†The normal mice were assumed to have a 100% normal prostate based on histologic analysis of separate mice.

‡Due to the large size of the high-grade primary tumors, the histologic classification for these tumors was estimated from three to five sections taken from the tumor.

§The percentage of necrosis for the late-stage tumors was estimated from the anatomic MR images because it was not practical to estimate it from the histology.